Master's Theses

Graduate College

12-1995

An Investigation of Turbulent Taylor-Couette Flow Using Laser Doppler Velocimetry in a Refractive Index Matched Facility

Joseph C. Parker

Follow this and additional works at: https://scholarworks.wmich.edu/masters_theses

Part of the Mechanical Engineering Commons

AN INVESTIGATION OF TURBULENT TAYLOR-COUETTE
FLOW USING LASER DOPPLER VELOCIMETRY IN A
REFRACTIVE INDEX MATCHED FACILITY

by

Joseph C. Parker

A Thesis
Submitted to the
Faculty of The Graduate College
in partial fulfillment of the
requirements for the
Degree of Master of Science
Department of Mechanical and
Aeronautical Engineering

Western Michigan University
Kalamazoo, Michigan
December 1995

ACKNOWLEDGEMENTS

There are many who have contributed toward the completion of this project. I must sincerely thank my advisor and mentor, Dr. Merati, for his direction and support. Without your help, I would not be in the position I am today. Thank you to Don Thompson for his office's financial contribution. Thank you to Glen Hall for teaching me the value of patience and fine craftsmanship. Thank you to the Center of Excellence for Fluid Mechanics Research for being my playroom of science and technology. Thank you to Jesus Christ for providing the tools and the hope.

I dedicate this final draft to my wife, Caryn Parker, who tirelessly helped me and supported me. You have provided more inspiration than you will ever know and I am deeply grateful. Thank you.

Joseph C. Parker

AN INVESTIGATION OF TURBULENT TAYLOR-COUETTE FLOW USING LASER DOPPLER VELOCIMETRY IN A REFRACTIVE INDEX MATCHED FACILITY

Joseph C. Parker, M.S.

Western Michigan University, 1995

Turbulent Taylor-Couette flow between an annulus formed by two concentric cylinders with dead end walls is comprised of complex patterns of vortices. An experimental apparatus was designed to provide refractive index matching between the annulus and working fluid. Optical access was maintained through three sides of the annulus and one end wall. An aqueous solution of sodium iodide was formulated to match the refractive index of the Plexiglas annulus. Laser Doppler Velocimetry was used to measure the three components of velocity and turbulence intensity throughout a planar section in the annulus. The annulus dimensions were: $\eta = 0.672$, $d = 15.08$ mm, and $\Gamma = 20$ and 4. The flow parameters were: $\Omega = 1200$ RPM, $T = 2.107 \times 10^9$, $T/T_c = 924,600$, and $Re = 73,440$. In the 20d/L annulus, 20 Taylor vortices were observed while 2 vortices were formed in the 4d/L annulus. Plots of radial-axial component velocity vectors and contour plots of component velocities and turbulence intensities reveal the Taylor vortex flow structure.

TABLE OF CONTENTS

LIST OF TABLES

LIST OF FIGURES

List of Figures - continued

INTRODUCTION

Flow in the gap between two concentric cylinders with one or both cylinders rotating has been examined and described since Maurice Couette in 1890 and Geoffrey Taylor in 1923 (Donnelly, 1991). At flow Taylor numbers above a critical value, the steady viscous flow becomes unstable due to perturbations, and alternating toroidal vortices develop as illustrated in Figure 1. As the rotational speed or Taylor number increases, the vortices can attain various mode shapes and transitions, becoming increasingly turbulent. Geometric dimensions, cylinder rotation, end wall effects, and fluid properties are some of the significant variables which define and maintain Taylor-Couette flow.

A measure of the state of flow is represented by the non-dimensional Taylor and Reynolds numbers. Taylor number, T, is defined as the ratio of centrifugal force to viscous force while Reynolds number, Re, is the ratio of inertia force to viscous force. Equation 1 is an expression for Taylor number as defined by Roberts (1965) while Equation 2 is a common expression for Reynolds number.

$$T = \frac{2\,\eta^2 d^4}{1 - \eta^2}\left(\frac{\Omega}{\nu}\right)^2 \tag{1}$$

$$Re = \frac{U_s d}{\nu} \tag{2}$$

where: $\eta = r_i/r_o$, the radius ratio

$r_i =$ inner cylinder radius

$r_o =$ outer cylinder radius

$d = r_o - r_i$, the gap width

$\Omega =$ inner cylinder angular velocity

$\nu =$ kinematic viscosity of the fluid

$U_S = r_i \, \Omega$, the circumferential speed of the inner cylinder surface

Figure 1. Taylor Vortices (Swinney & Gollub, 1985).

Source: Swinney, H. L., & Gollub, J. P. (1985). Hydrodynamic instabilities and the transition to turbulence (2nd ed.). New York: Springer.

The critical Taylor number, T_c, identifies the onset of instability and the point at which Taylor vortices form. The Taylor number ratio T/T_c is used to reference the flow regimes which are classified under subcritical, critical, and supercritical Taylor number. Turbulent Taylor vortices exist at Taylor numbers greater than $1000T_c$ (Koschmieder, 1993).

Because Taylor-Couette flow exists in an annulus formed by two concentric cylinders, accurate velocity and turbulence intensity measurements using a physical probe can be difficult to obtain without disturbing the flow. Laser Doppler Velocimetry, however, is a non-intrusive technique which is used to measure mean velocity and turbulence intensity through an optical window. Although an annulus can be constructed from clear acrylic, the cylindrical surfaces introduce refraction effects which can be difficult to overcome. If the outer cylinder consists of a cylindrical hole through an acrylic block and if the working fluid has the same refractive index as the acrylic, light refraction exists only on the outer flat surface and not at the fluid-acrylic interface. This technique is called refractive index matching and it allows the laser beams to probe the entire annulus with complete optical freedom. Even boundary layer measurements on the inner and outer cylinder walls are attainable.

The primary focus of this research was the investigation of supercritical, turbulent Taylor-Couette flow in a refractive index matched annulus with the inner cylinder rotating. Laser Doppler Velocimetry was used to measure the three components of mean velocity turbulence intensity. Symmetry conditions of the mean

radial and axial velocity were examined for different circumferential planes. Data was collected for both a long and short annulus, where the influence of the end walls was investigated.

LITERATURE REVIEW

Taylor-Couette Flow

Publications exist for all states of Taylor-Couette flow and include theoretical, experimental, and numerical investigations. Particular attention was focused on the transition from stable to unstable flow and the defining parameters. Sparrow, Munrow, and Jonsson (1964) and Walowit, Tsao, and DiPrima (1964) calculated the critical Taylor number, T_c, as a function of cylinder radius ratios by solving linearized momentum equations. Roberts (1965) solved the equations of motion with small perturbations superimposed on the mean flow and calculated the critical Taylor number for various operating conditions. Roberts' (1965) definition of Taylor number (Equation 1) and numerical calculations of the critical Taylor number were used in this research because of their frequent reference by other publications. By normalizing the operating Taylor number as a ratio with respect to T_c, the flow regime is easily distinguishable and comparisons of results can be made without regard to the particular Taylor number definition used.

Leading up to and including the turbulent regime, the literature includes high quality flow visualization photographs which display the various modes of vortex formation. Burkhalter and Koschmieder (1973) studied Taylor vortex wavelength and the size of the end wall rings as the gap width, radius ratio, end conditions, and fluids

were altered. Their photographs included Taylor number ratios from 0.99 to 11,330. In Burkhalter and Koschmieder (1974), the effects of start-up conditions on the supercritical vortices were examined. In experiments involving Taylor number ratios up to 11,000, they concluded that the Taylor vortex mode is dependent on the cylinder's rotational acceleration.

Smith and Townsend (1982) used hot-wire anemometry and pitot tubes to measure flow velocity and turbulence intensity in a turbulent Taylor-Couette flow between the range $1.0 \times 10^4 < T/T_c < 2.3 \times 10^6$. Because the toroidal vortices are stationary, a small axial flow was introduced to push the vortices past the stationary probe. It was concluded that the toroidal eddies lose their regularity at very high rotation rates and cannot be clearly distinguished at Taylor number ratios greater than 5×10^5.

Fenstermacher, Swinney, and Gollub (1979) used Laser Doppler Velocimetry to measure the local radial velocity in a chaotic Taylor vortex flow. Although the laser system was aligned to measure the system axial velocity, the vortex radial velocity with respect to its center was recorded. The measurements were limited to an axial line passing through the vortex centers, along $r = (r_i + r_o)/2$.

Barnes, Flitney, and Nau (1992) proposed a Taylor vortex flow pattern in a generic seal chamber which acted to wear the inner and outer cylinders at the radial inflow and outflow regions. The investigation focused on the design of an optimum seal chamber which reduces the vortex effects and adds other flow features.

Merati, Parker, and Adams (1992) investigated the flow within an ANSI enlarged seal chamber with a rotating impeller on one annulus end and a stationary wall on the other end. It was concluded that one large vortex occupied the chamber and the flow was non-symmetric. Unpublished research by Merati (1995) includes research in a seal chamber with a close clearance throat restriction at the impeller end and a stationary wall at the other end. It is expected that the closed annulus will provide a new combination of Taylor vortex shapes.

The results of this research fall under the category of providing a link between several approaches to Taylor-Couette flow investigations. Mechanical seal chamber studies can benefit from the short annulus results for which both end walls are stationary. In addition, qualitative data for the long annulus case can be used to further turbulent Taylor-Couette flow theories.

Refractive Index Matching

Different approaches to refractive index matching are present in the literature and most are unique in terms of application and the selection of solid and liquid materials. Braun, Canacci, and Hendricks (1990) reported using a mixture of Dow Corning mineral silicone oil 556 and Dow Corning mineral oil 550 at 25 C to match the refractive index of Plexiglas. Similarly, Northrup, Kulp, and Angel (1991) used a mixture of Dow Corning mineral oil 550 and Union Carbide organosilicone L42. Both of these fluid combinations, although inert, have high viscosities and would provide low

Taylor number ratios. Thompson (1990) used a mixture of Tetralin and steam-distilled turpentine in a Plexiglas facility. Although low viscosities were reported, the solvent mixture softened and crazed the Plexiglas, reducing the model life. Chen and Kadambi's (1990) experiments with aqueous solutions of sodium iodide found a wide range of refractive indices and the ability to match the refractive index of silica gel (n=1.443). By varying the concentration of sodium iodide up to 60 percent by weight and the solution temperature from 20 to 40 C, the refractive index ranged from 1.333 to 1.487. With such a widely adjustable refractive index, the monitoring and control of the fluid concentration and temperature is critical.

Dybbs and Edwards (1987) evaluated the need for a close match of indices when curved interfaces are encountered by asking the question "n_1/n_2: How close is close enough?" where n_1 and n_2 are the refractive indices for the solid medium and the fluid, respectively. For a horizontal ray intersecting a curved interface as in Figure 2, if the ratio $n_1/n_2 = 1.0$, then the incident angle, θ_1, equals the refraction angle, θ_2. Geometry provides a relationship for θ_1 as expressed in Equation 3 while Snell's law provides a relationship between the incident and refracted angles as in Equation 4.

$$\sin(\theta_1) = \frac{h}{R} \qquad (3)$$

$$n_1 \sin(\theta_1) = n_2 \sin(\theta_2) \qquad (4)$$

such that

$$\theta' = \sin^{-1}\left(\frac{h}{R}\right) - \sin^{-1}\left(\frac{n_1}{n_2}\frac{h}{R}\right) \qquad (5)$$

where θ' is the angular deviation from the horizontal, R is the cylinder radius, and h is the ray height from horizontal. For applications where h/R approaches unity, the refractive index ratio becomes critical. In addition, by monitoring n_1/n_2, the angular deviation can be predicted.
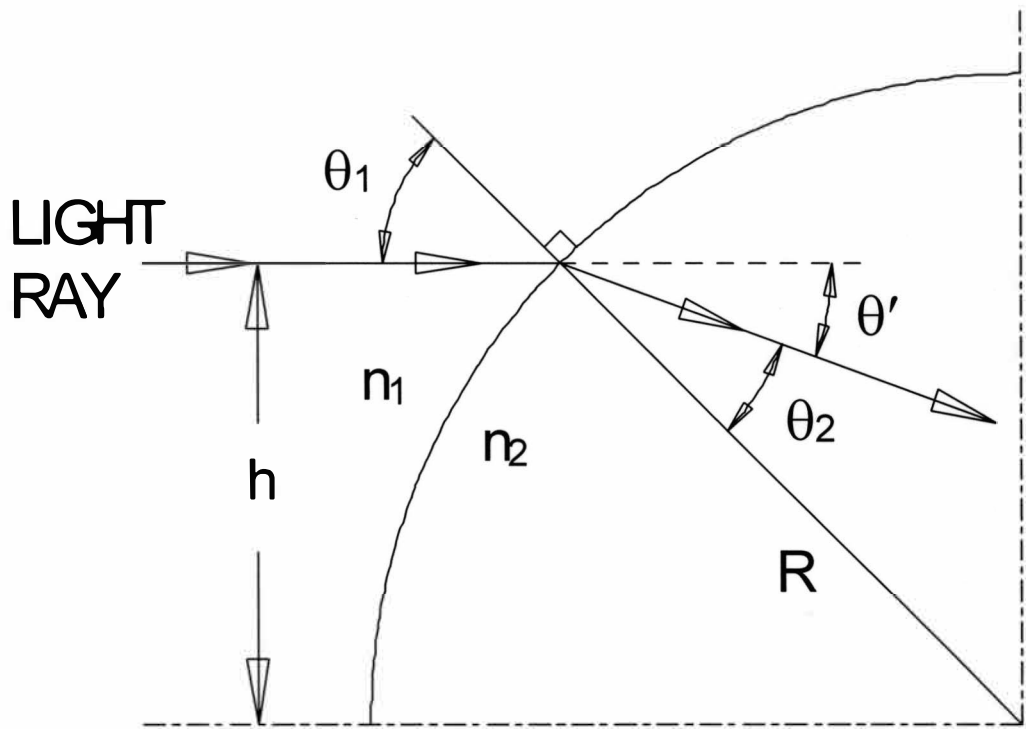

Figure 2. Horizontal Ray Intersecting a Curved Interface of Radius R.

EXPERIMENTAL PROCEDURES

Experimental Apparatus

A schematic of the Taylor-Couette flow test apparatus is shown in Figure 3. The working fluid is located in the annulus region confined between two vertically aligned concentric cylinders and two end walls. Fluid inlet and outlet taps are located at each end of the annulus for fluid changes and the removal of trapped air. Only the shaft and inner cylinder are free to rotate.

The inner cylinder is a clear acrylic sleeve fixed to a stainless steel shaft at the upper end and centered by a bushing on the lower end. The shaft is suspended by two consecutive pillow blocks at the upper motor coupling end and retained by a low friction bushing at the lower end. The inner cylinder design facilitates the installation of different diameter sleeves. The outer cylinder is a cylindrical bore through a solid 15.24 x 15.24 x 34.67 cm block of clear Plexiglas. To reduce the effects of non-uniform geometry, a radial tolerance of ±0.025 mm was maintained for the inner and outer cylinders. Shaft eccentricity was measured at less than ±0.038 mm at the lower end of the shaft.

Elastomeric Coupling

Pillow Blocks

Upper Chamber

Mechanical Seals

Fluid Inlet

Upper End Wall

Outer Housing

Inner Cylinder

Thermocouple Port/
Fluid Outlet

Spacer

Teflon Bushing

Lower End Wall

768.35
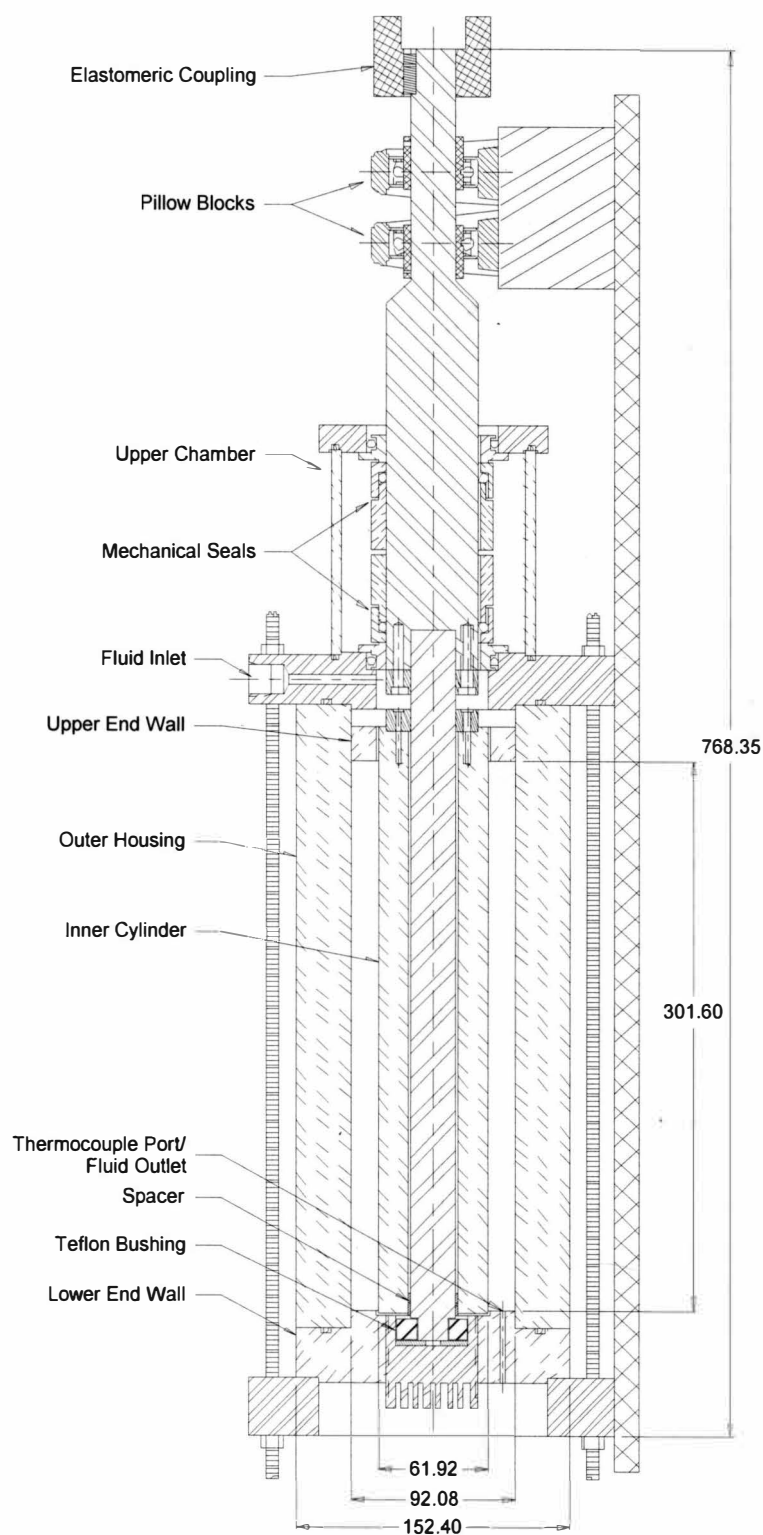
301.60

61.92

92.08

152.40

Figure 3. Section Through the Apparatus. (All dimensions in mm.)

The upper and lower end walls were also machined from clear Plexiglas so as not to block the laser beams from measurements in the end wall boundary layers. The lower end wall acts to retain the lower shaft end from radial movement and provides optical access from below. What is referred to as the upper end wall is a rectangular ring with close clearances to the inner and outer cylinder diameters. Annulus length is adjusted by changing the length of four steel rods which are fastened between the ring and the upper structural plate. The upper end wall is retained in a rigid fashion such that the rotating inner cylinder and moving fluid do not induce any measurable relative motion. All acrylic surfaces were polished to obtain excellent optical clarity and annealed to relieve residual stresses.

Testing was performed for cylinders with r_i = 30.96 mm and r_o = 46.04 mm, providing a gap width d = 15.08 mm and radius ratio η = r_i/r_o = 0.672. These dimensions are characteristic of the inside diameter of an ANSI B73 standard enlarged cylindrical seal chamber and the outside diameter of a Durametallic 48.0 mm CBR Dura Seal (bellows-type mechanical seal). The aspect ratio, Γ, is defined as the ratio of the annulus length to the gap width and was set to 20 and 4. For Γ = 20, the annulus length was 301.6 mm, and for Γ = 4, the annulus length was 60.32 mm.

A variable speed motor with a maximum 1750 rpm and accuracy of +/- 1.0 rpm was connected inline with the stainless steel shaft through an elastomeric coupling. The entire system was mounted to a rigid bracket and fixed vertically to a rigid wall.

Leveling control was provided for all axes. With accurate shaft alignment, vibrations were minimized and did not affect the quality of results.

Leakage paths between stationary components were sealed with o-rings while mechanical seals blocked the leakage paths between rotating and stationary interfaces at the upper end. A separate chamber housing two mechanical seals was flushed with cooling water for the transfer of heat generated at the seal faces. Although the heat generated at the lower bearing was insignificant, an aluminum boot was designed with heat sink fins to remove any frictional heat. Access for a thermocouple was provided axially through the lower end wall such that its position could be adjusted to measure the temperature distribution throughout the length of the annulus. After the entire system reached a steady state equilibrium, a maximum temperature gradient of 2.0 C was measured along the annulus.

Refractive Index Matching

Plexiglas acrylic has an index of refraction of 1.4905 for 514.5 nm wavelength light at 23.4 °C. The refractive index of solid sodium iodide is 1.7745 and at its saturation concentration of 64.8% by weight in water, the solution refractive index is 1.5025. With the saturated solution as the starting point, water can be added to match the refractive index of Plexiglas. Because the refractive index is susceptible to temperature, if the operating temperature is known and can be controlled, the mixture concentration can be used to iterate on the best refractive index match. The cooling

provided at the annulus ends established a steady state temperature of 26.7 C at the lower annulus end and 28.7 C at the upper end. A Spencer Abbe-type refractometer measuring off the sodium D line with a white light source was used for refractive index measurements at the matching temperature.

Sodium iodide releases iodine upon prolonged exposure to light and the fluid turns a brownish color. This effect can be counteracted by the addition of small amounts of sodium thiosulfate. Also, upon exposure to air, the mixture slowly crystallizes and can extrude through the smallest crevices, leaving yellow-stained trails.

For the sodium iodide mixture, the viscosity was measured as $\nu = 1.47$ centipoise at 26.7 C and the density was 1.84 gm/cc. The refractive index was maintained at 1.4905 ± 0.0005 for all tests. The index ratio of the acrylic to the fluid falls between $1.0003 < n_1/n_2 < 0.9997$. Following the format of Figure 2, if an incoming light ray passes through the cylinder at an eight degree angle with respect to the horizontal and exits at the topmost horizontal tangent to the cylinder, the maximum θ_2 is 82 degrees. It can then be shown that $h/R = \sin(82)$. From Equation 4, the expected experimental angular deviation off the horizontal was $\theta' = 0.28\%$.

For the radius ratio $\eta = 0.672$, Roberts (1965) calculated the critical Taylor number as $T_c = 2279$. At an experimental rotational speed of 1200 rpm, the Taylor and Reynolds numbers were $T = 2.107 \times 10^9$ and $Re = 73,440$, respectively, and the Taylor number ratio was $T/T_c = 924,600$.

Preparation Procedures

For each test, the same start-up procedures were followed to ensure repeatable results. The sodium iodide solution was introduced to the annulus through a port in the lower structural plate, displacing the initial volume of air through a port in the upper structural plate. The variable speed motor was cycled through several speeds and the residual trapped air was released. The motor was then fixed at the desired rotational speed for at least 30 minutes such that an equilibrium fluid temperature of 27.7 C was reached. Rotational speed was measured by a calibrated strobe light. The fluid temperature and inner cylinder speed were monitored frequently throughout the experiments.

Laser Doppler Velocimetry Measurements

A one component Laser Doppler Velocimetry (LDV) system was used to measure all three components of velocity and turbulence intensity along a radial-axial plane in the annulus (see Figure 4). LDV is a non-intrusive technique for the investigation of flow structures in fluids. It takes advantage of the coherent properties of a laser by creating a fringe pattern at the intersection of two identical beams. This fringe pattern takes the form of an ellipsoid-shaped measurement volume and is maneuvered into the flow such that particles in the flow pass though the measurement volume. As a particle travels through the fringes, it scatters photons at a frequency proportional to the particle velocity. By collecting the scattered photons with a

photodetector, the frequency and therefore particle velocity can be measured for the component in the plane of the beams. In addition, frequency shifting is used to determine the direction of flow.

LDV is a time-averaging technique such that thousands of burst samples are recorded and averaged at each sampling location. Data rate and data density are important characteristics of the technique and care must be taken to ensure that the measured mean velocity is indicative of the true mean flow and not an arbitrary set of signal bursts. Metallic coated, 4.0 μm diameter spherical particles were used in the flow as scattering particles. Although these particles provided a decent signal-to-noise ratio,
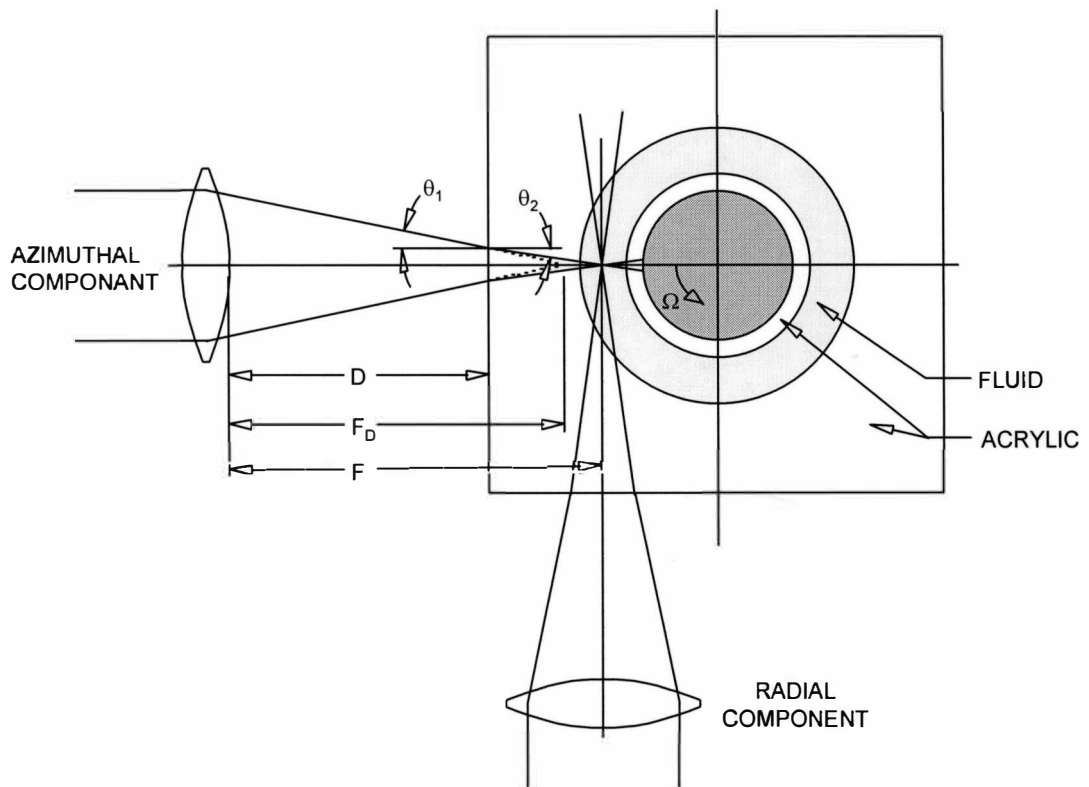

Figure 4. Beam Arrangement for Azimuthal and Radial Component Measurements.

they agglomerated in the sodium iodide mixture in approximately 48 hours and turned the fluid cloudy. At this point, the fluid needed to be changed.

Azimuthal and radial velocities on the radial-azimuthal plane are defined as shown in Figure 4. The axial velocity, defined positive up along the axis of rotation, was measured with the laser beams parallel to the radial-axial plane. The planar outside surface of the housing avoids asymmetric refraction of the laser beams as they pass into the chamber. Because the housing and fluid have approximately equal refractive indices, the laser beams encounter refraction only at the flat housing surface. Snell's law (Equation 5) was used to predict the location of the measurement volume within the annulus. In this case, $n_1 = 1.0$ for air and $n_2 = 1.4905$ for the acrylic and the working fluid.

Because $n_1 \neq n_2$ and $\theta_1 \neq \theta_2$, with respect to Figure 4, the focal distance from the lens to the measurement volume located in the medium is different than the virtual measurement volume location for $\theta_1 = \theta_2$. The new focal distance, F, can be calculated through a simple manipulation of Snell's law and the geometric characteristics.

$$F = F_D \frac{\tan \theta_1}{\tan \theta_2} + D \left[1 - \frac{\tan \theta_1}{\tan \theta_2} \right] \tag{6}$$

where F_D is the focal distance in air and D is the distance from the front of the lens to the window.

A 23.5 mW argon-ion laser with 514.5 nm wavelength was used with a 122.19 mm focal distance focusing lens. This lens and a 50 mm beam separation provided a half angle $\theta_2 = 7.729°$, measurement volume length of 0.330 mm, diameter of 0.045 mm, and fringe spacing of 1.28 μm in the fluid.

RESULTS

The primary results of this research were experimental measurements of the three mean velocity components u_r, u_z, and u_θ and their respective Root Mean Square values of the fluctuations u_r', u_z', and u_θ'. Measurements in the $\Gamma = 20$ annulus were obtained only in the lower third of the chamber such as to concentrate on the extent of the end wall effects. In addition, trapped air bubbles remained in the upper third region of the annulus and could have added uncertainty to the measurements. For the $\Gamma = 4$ case, the entire annulus was investigated. Data was recorded at 1.0 mm radial intervals and 2.0 mm axial intervals on the primary $\theta = 0$ plane. For flow symmetry investigations, data was recorded at 1.0 mm radial intervals and 10.0 mm axial intervals on the $\theta = \pi$ plane. Average component velocity and turbulence intensity was compiled from 2048 samples at each measurement location. Data was recorded in the boundary layer at the inner and outer cylinders; however, the finite size of the probe volume and poor signal-to-noise ratio prohibited fine detail in these regions.

Radial-Axial Velocity Vectors

Velocity vectors of radial and axial component velocities are presented in Figures 5 and 6 for the $\Gamma = 20$ and $\Gamma = 4$ annulus cases, respectively. All velocities are non-dimensional with respect to the inner cylinder surface speed, $U_S = 3.89$ m/s.
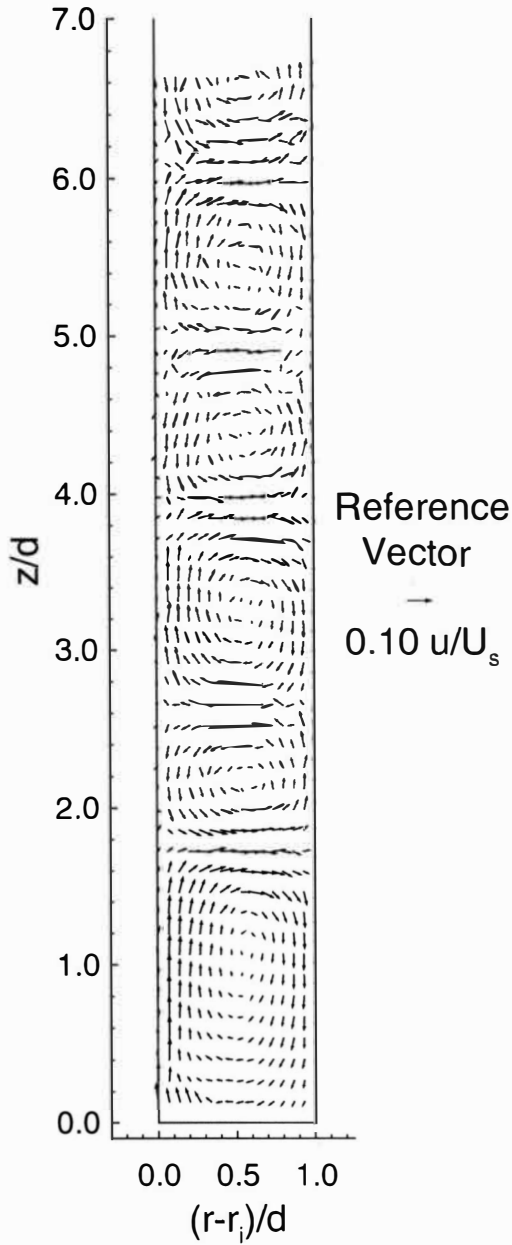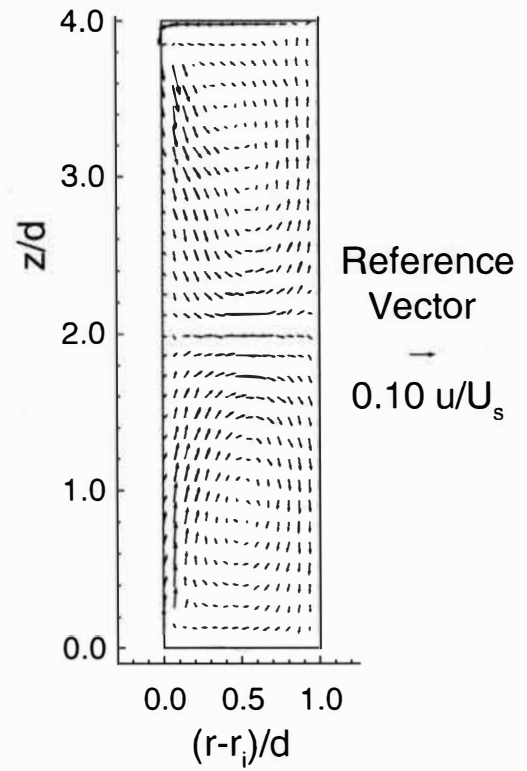
Figure 5. Radial-axial Velocity Vectors,
$\Gamma = 20$.

Figure 6. Radial-axial Velocity Vectors,
$\Gamma = 4$.

The radial and axial scales are non-dimensional with respect to the annulus gap. While the $\Gamma = 4$ case was neatly split into two equal vortex regions, the $\Gamma = 20$ case had 18 vortices in the complete annulus. A symmetry plane at L/2 was observed for both cases. The vortex center of the top vortex for the $\Gamma = 4$ annulus is offset toward the inner cylinder and end wall corner due to the leakage of fluid around the edges of the upper end wall ring. Future experiments will consider eliminating the gap and thus eliminate this consequence. End wall effects are apparent in both cases such that the vortices closest to the end walls are elongated. The inward radial component at the end walls agrees with the conclusions of Koschmieder (1993) for a very long annulus and with Merati, Parker, and Adams (1992) for a short annulus.

Taylor vortices are commonly sized by their wavelength, λ, which is a ratio of the axial length of a pair of vortices divided by the gap width. Typically, wavelength refers to the average Taylor vortex pair size over the entire annulus. Because of the relatively short annulus lengths for which data was recorded, the half wavelength, $\lambda/2$, was measured for each vortex and is summarized in Table 1. The half wavelength was measured as the distance between radial outflow and inflow regions, defining one vortex. This approach illustrates the extent of end wall effects through the annulus length. Vortex numbering starts at the lower end wall and increases in the axial direction. The first three vortices for the $\Gamma = 20$ case are directly affected by the stationary end wall and each appear to illustrate the transitional stages required to stabilize the radial velocity pattern. Considering the vortices as pairs, the first set is

composed of an elongated vortex 1 and a condensed vortex 2. Likewise, the second set consists of vortex 3 longer than vortex 4. In vortex 1, the radial inflow borders the stationary end wall while the radial outflow borders a mating vortex. Consequently, vortex 1 settles into an elongated shape. Vortex 2 compensates for its elongated partner by reducing its size such as to minimize the unit's total length. Similarly, vortex 4 compensates for vortex 3. With the critical wavelength for this flow numerically predicted at $\lambda_c = 2.00$ by Roberts (1965), the local wavelength converges to the critical local wavelength from above as the distance from the end wall increases. The local wavelengths for vortices greater than 5 are expected to remain at 1.06 because of the lack of end wall influence. Literature firmly reports that the wavelength for supercritical vortices is greater than the critical wavelength (Koschmieder, 1993), which confirms the 0.06 experimental difference.

Table 1

Measured Vortex Size as a Function of Annulus Length

| | Local Wavelength, $\lambda/2$ | |
Vortex Number	$\Gamma = 20$	$\Gamma = 4$
1	1.72	2.0
2	0.86	2.0
3	1.33	
4	1.06	
5	1.06	

Component Velocity Profiles for the $\Gamma = 20$ Annulus

Contours of radial, axial, and azimuthal velocity are plotted in Figures 7 through 9, respectively, for the $\Gamma = 20$ annulus. Positive component directions are parallel to the component axes and with positive azimuthal velocity directed into the page. For the sake of velocity gradient definition, the contour ranges were enhanced in the midrange sections.

The maximum radial velocity occurs in the radial outflow regions on adjacent vortices. Centrifugal forces act to increase the outward radial velocity in these regions and impede the returning flow. The axial velocity contours show that the zero velocity point in the radial direction is located at approximately $(r-r_i)/d = 0.6$. This offset from the annulus radial center is also be attributed to the centrifugal forces acting to throw fluid away from the inner cylinder.

Up to this point, flow only on the radial-axial plane has been discussed and without considering the circumferential dimension, the rectangular Taylor vortex cells (with respect to the radial-axial plane) might be regarded independent of the rotating inner cylinder. With the inclusion of the azimuthal velocity, the flow picture becomes much more complex with respect to through-plane activities. Figure 9 maps contours of azimuthal velocity revealing a significant gradient along the radial axis. Although boundary layer measurements were not possible on the inner and outer cylinders, the azimuthal velocity drops rapidly from the inner cylinder surface speed at the inner
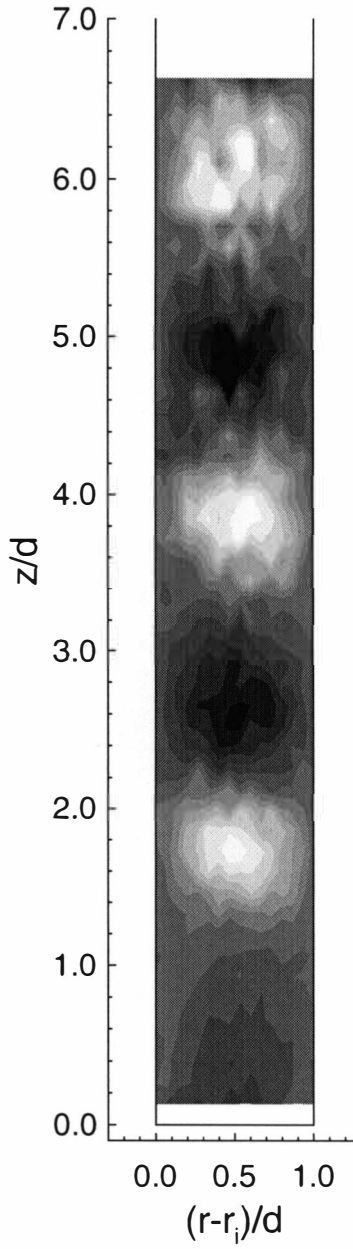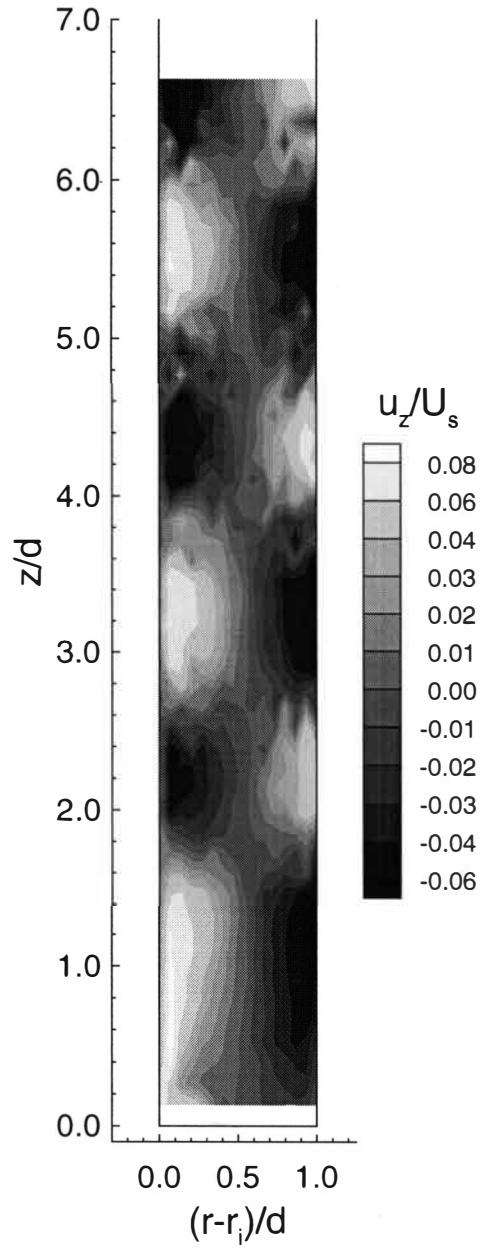
Figure 7. Radial Velocity, $\Gamma = 20$.
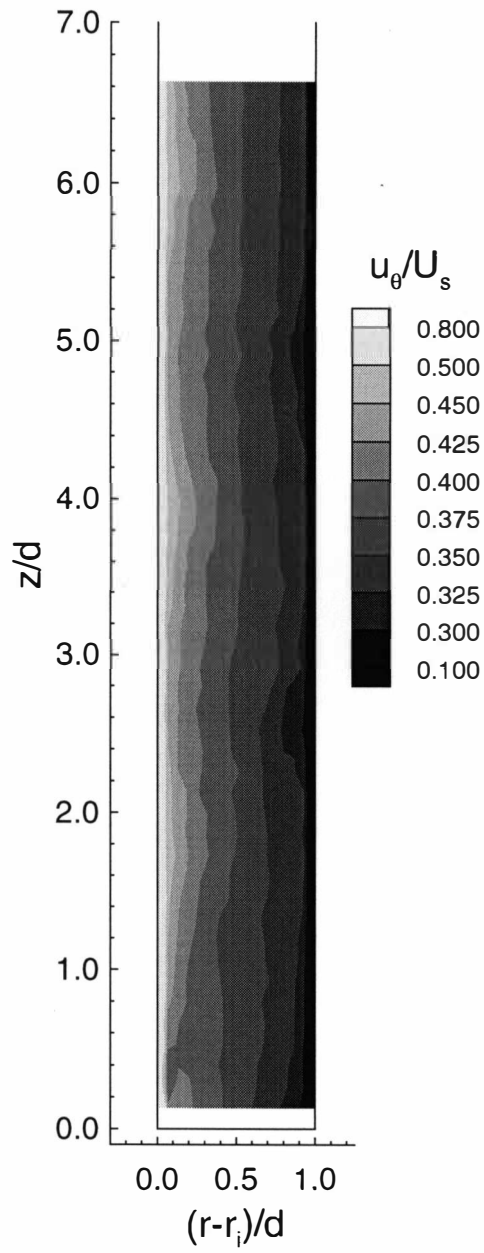

Figure 8. Axial Velocity, $\Gamma = 20$.

Figure 9. Azimuthal Velocity, $\Gamma = 20$.

cylinder ($u_\theta/U_s = 1.0$) and ends with zero velocity at the outer cylinder. Over 80% of the mean flow u_θ/U_s is between 0.5 and 0.3.

With respect to the radial-axial velocity vector plots, the fluid at the inner cylinder is moving into the page 12.5 times faster than the axial velocity and does not move into the page at the outer cylinder. Therefore, not only are the fluid particles rotating about their vortex centers while they move in the azimuthal direction, but they also follow an azimuthal shearing gradient between the inner and outer cylinders.

Inspection of the azimuthal velocity plots reveals regions of extended velocity gradient which coincide with the constructive radial outflows at the inner cylinder and inflows at the outer cylinder. Merati, Jacobs, and Parker (1995) described the azimuthal velocity gradient in terms of jet flow: "The regions between the adjacent vortices behave similar to jet flow in redistributing the high speed azimuthal flow near the inner cylinder and the low speed flow near the outer cylinder. In the regions where there is outflow toward the stationary outer cylinder, high speed azimuthal flow is directed toward the outer stationary cylinder. In the regions where the jet flow is toward the inner rotating cylinder, the slow flow is directed toward the inner cylinder."

Component Velocity Profiles for the $\Gamma = 4$ Annulus

Contours of radial, axial, and azimuthal velocity are plotted in Figures 10 through 12, respectively, for the $\Gamma = 4$ annulus. The radial and axial contours again
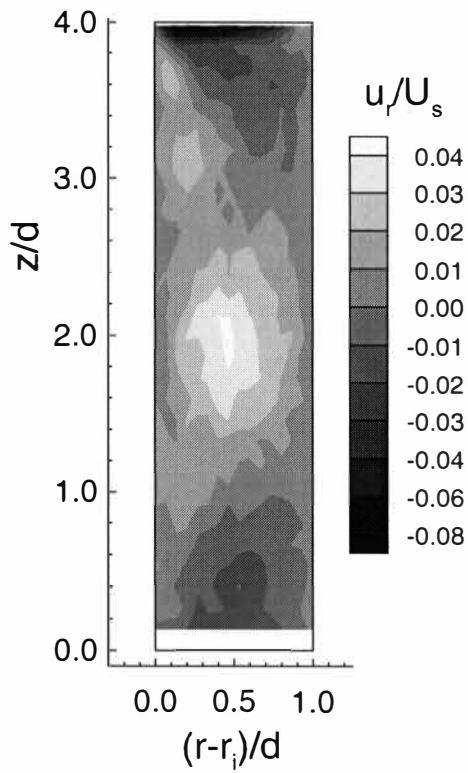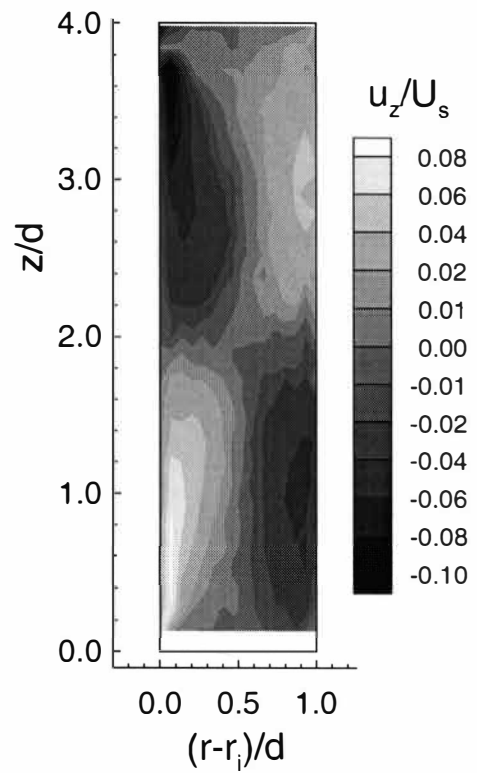
Figure 10. Radial Velocity, $\Gamma = 4$.
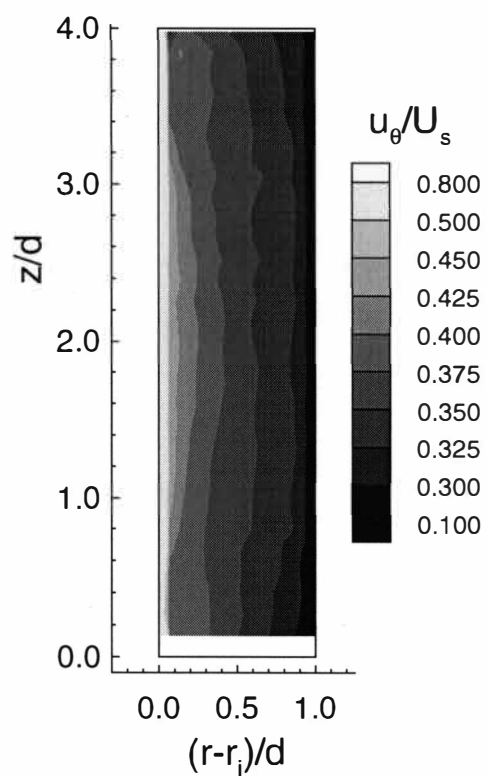

Figure 11. Axial Velocity, $\Gamma = 4$.

Figure 12. Azimuthal Velocity, $\Gamma = 4$.

reveal the circulation of fluid around the upper end wall ring. The two vortices are similar in structure to the first vortex for the $\Gamma = 20$ annulus. The maximum radial velocity at the radial outflow region is half the velocity for the $\Gamma = 20$ case. In addition, the radial velocity at the lower end wall is half the velocity for the $\Gamma = 20$ case. The axial velocity at the inner cylinder is comparable to the $\Gamma = 20$ case, but at the outer cylinder it is again only half the $\Gamma = 20$ value. The stationary end walls act to slow the complete rotational vortex flow except for the radial component at the inner cylinder.

The azimuthal velocity also resembles the $\Gamma = 20$ case such that the azimuthal velocity compensates for a jet flow effect at the radial outflow region at $z/d = 2.0$. In the radial inflow regions along the end walls, the slow azimuthal flow is similarly directed toward the inner cylinder.

Turbulence Intensity for the $\Gamma = 20$ Annulus

Turbulence intensity is defined as the standard deviation of the mean velocity divided by a characteristic velocity. For Taylor-Couette flow, the inner cylinder surface speed U_S is used. Standard deviation is essentially an average variation of the instantaneous velocity with respect to the mean flow. With the Reynolds number at 73,440, the component velocities are by definition turbulent.

Contours of turbulence intensity for the radial, axial, and azimuthal velocity components in the $\Gamma = 20$ annulus are shown in Figures 13 through 15, respectively.
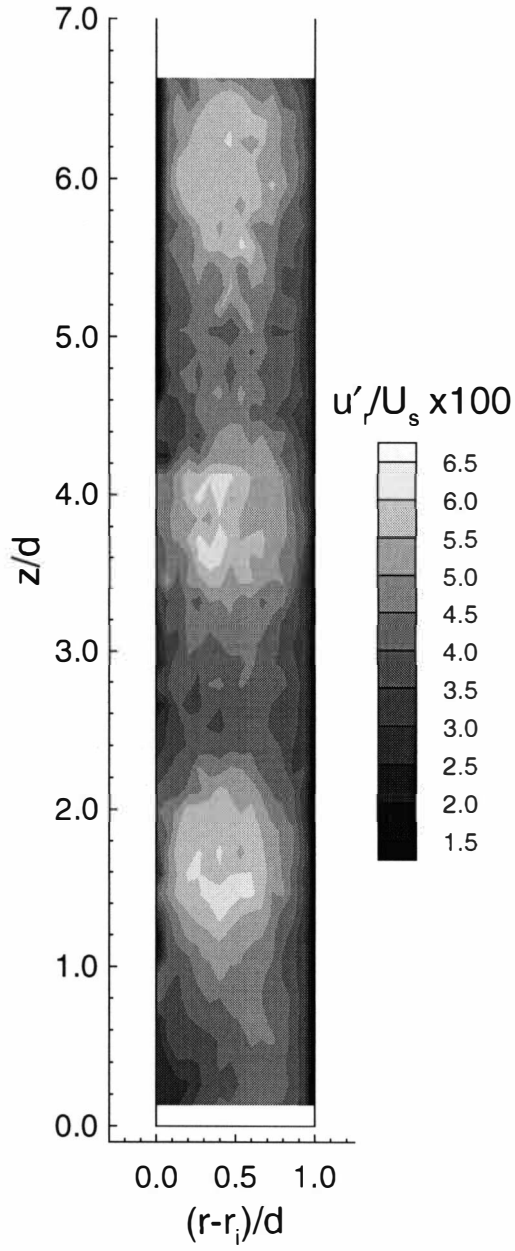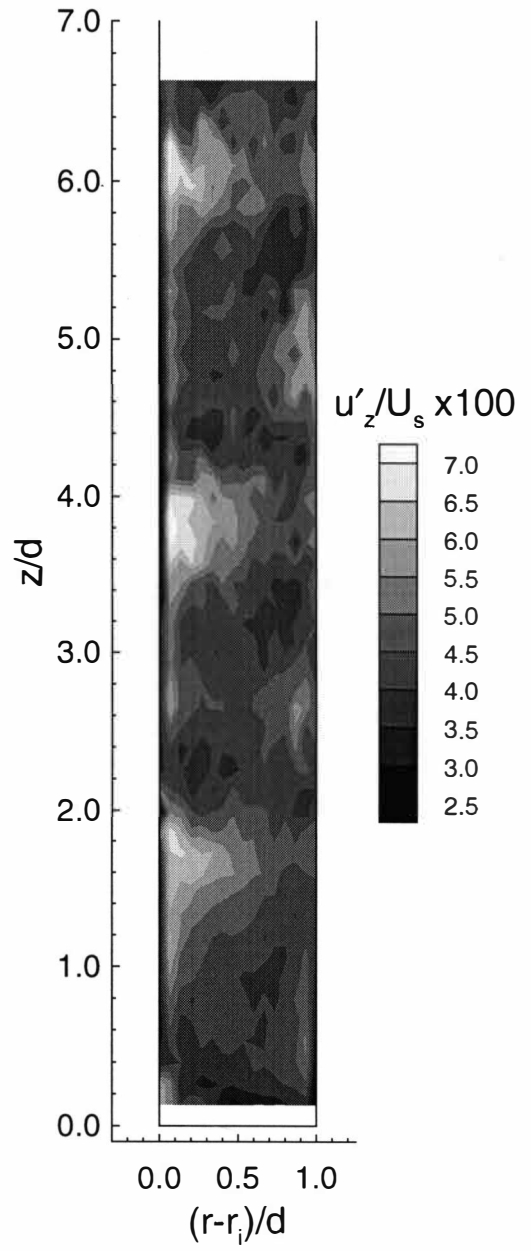
Figure 13. Radial Turbulence Intensity, $\Gamma = 20$.
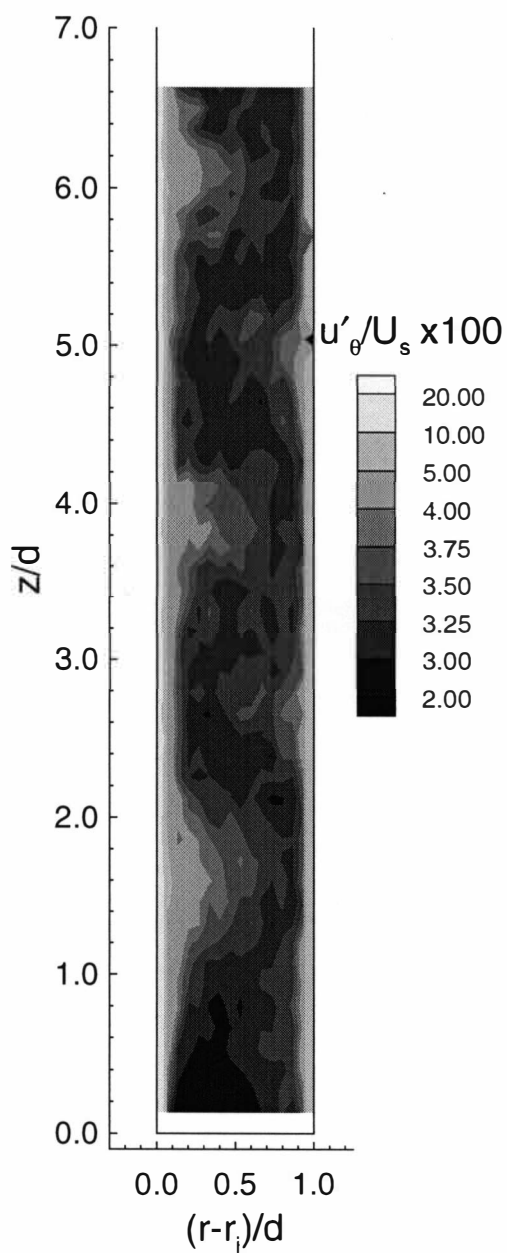
Figure 14. Axial Turbulence Intensity, $\Gamma = 20$.

Figure 15. Azimuthal Turbulence
Intensity, $\Gamma = 20$.

These contours show that the observed Taylor vortices are turbulent for these Taylor and Reynolds numbers.

Large azimuthal velocity gradients in the boundary layers near the inner and outer cylinders generate more turbulence in the azimuthal direction compared with the rest of the annulus flow. The jet flow structures produced by the Taylor vortices not only distribute the mean flow contours but also the turbulence intensity contours. Since more turbulence exists near the inner cylinder due to its larger shear layer, larger zones of high azimuthal turbulence intensity occur at the radial outflow regions near the inner cylinder.

The dominant turbulent flow near the inner cylinder affects the radial and axial turbulence intensity contours as shown in Figures 13 and 14, respectively. Larger zones of high turbulence intensities for the radial and axial components occur at the radial outflow regions at the center of the gap and near the inner cylinder, respectively.

Turbulence Intensity for the $\Gamma = 4$ Annulus

Figures 16 through 18 display contours of turbulence intensity for the radial, axial, and azimuthal velocity components, respectively, in the $\Gamma = 4$ annulus. The same jet flow arguments presented for the $\Gamma = 20$ case can be applied to the $\Gamma = 4$ case. In fact, the contours are very similar for any selected set of two vortices for the $\Gamma = 20$ annulus.
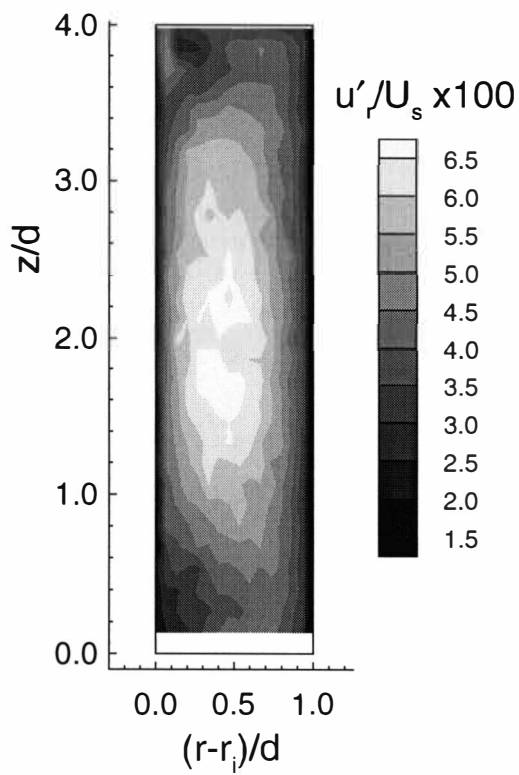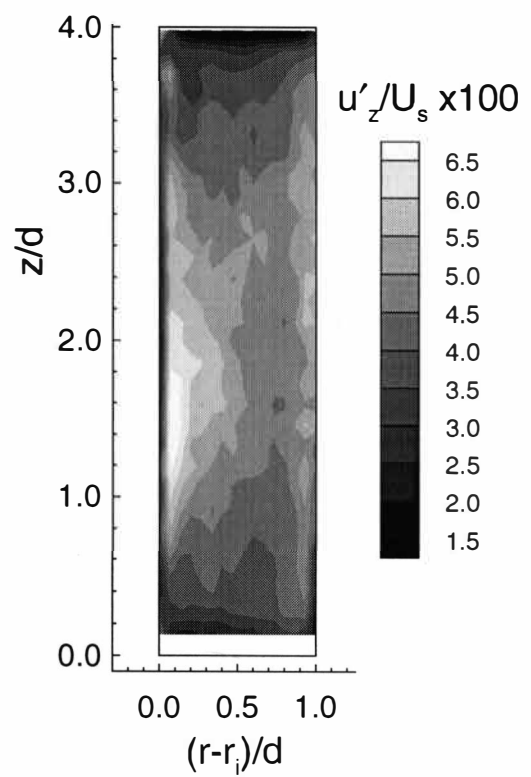
Figure 16. Radial Turbulence Intensity, $\Gamma = 20$.
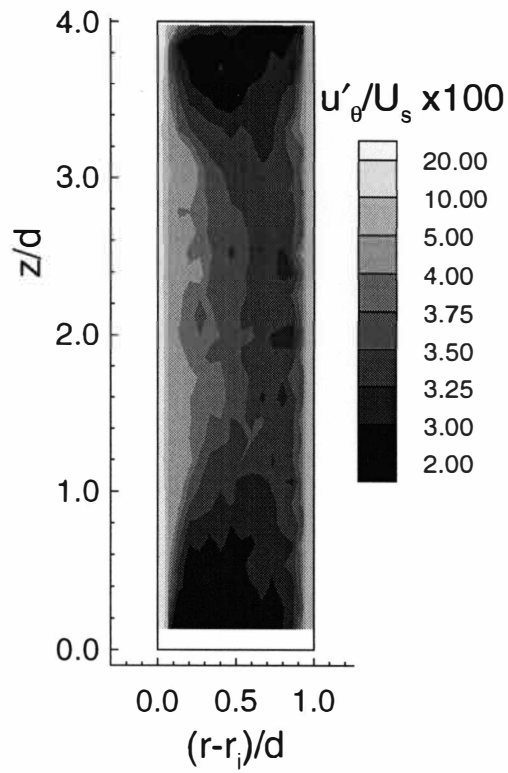
Figure 17. Axial Turbulence Intensity, $\Gamma = 4$.

Figure 18. Azimuthal Turbulence
Intensity, $\Gamma = 4$.

Investigation of the Flow Symmetry

Proving the existence of symmetry in the azimuthal direction reduces the need to map the entire three-dimensional annulus. In the $\Gamma = 20$ annulus, the primary and secondary planes are separated by 180 degrees and are referred to as $\theta = 0$ and $\theta = \pi$, respectively. Azimuthal velocity, the dominant component, was assumed to follow symmetry and was not measured at $\theta = \pi$.

Velocity vectors of axial and radial component velocities are presented in Figure 19. The vectors are presented in the same planar coordinate format as in Figure 5 even though the true radial direction is the inverse. The vector plots qualitatively show very similar vectors for equivalent measurement locations.

Figures 20 through 30 present incremental plots of the radial and axial velocity magnitudes for each plane at each z/d location. While the trends show some random variations, the velocities are in general very similar between circumferential planes. At z/d locations where the radial or axial velocity reaches a maximum or minimum, the correlation is excellent. For example, the radial velocities at z/d = 0.13 and the axial velocities at z/d = 0.66 follow each other closely. At z/d locations less than 4.0, the velocity correlations are best. In measurements above z/d = 4, however, increasingly large discrepancies between the theta planes are prevalent. This result may be due to the loss of vortex regularity reported by Smith and Townsend (1982) for very high Taylor number ratios.
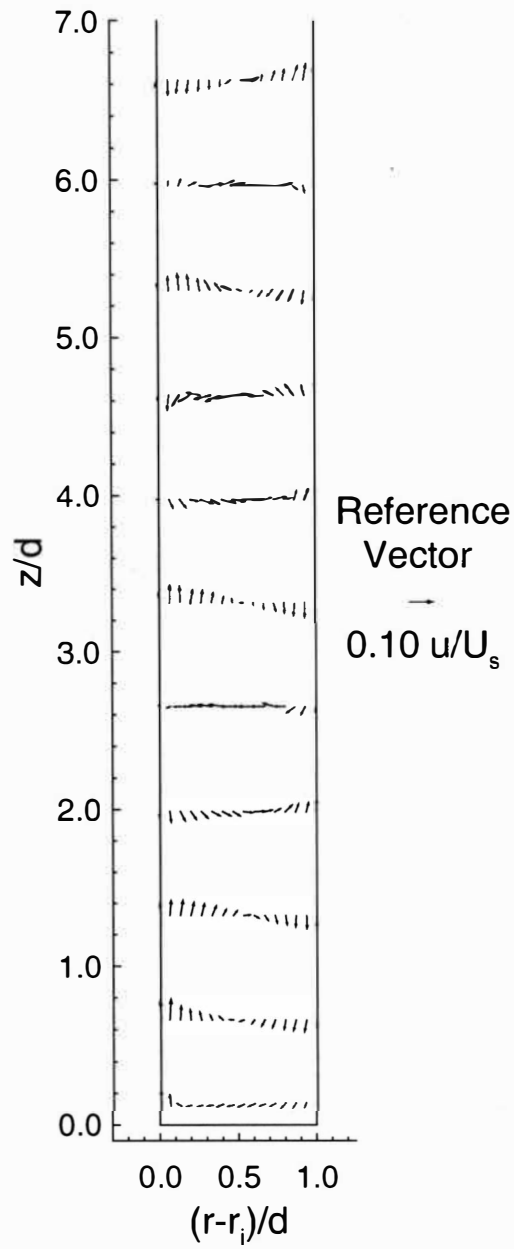
Figure 19. Radial-axial Velocity Vectors,
$\Gamma = 20$, $\theta = \pi$.

A primary focus of this research was to investigate the effects of end walls on the Taylor vortices. In the region where $z/d < 4.0$, the overall quality of this comparison supports the axisymmetric behavior of the flow. Therefore, the axial, radial, and azimuthal velocities and turbulence intensities are assumed axisymmetric through the circumference.
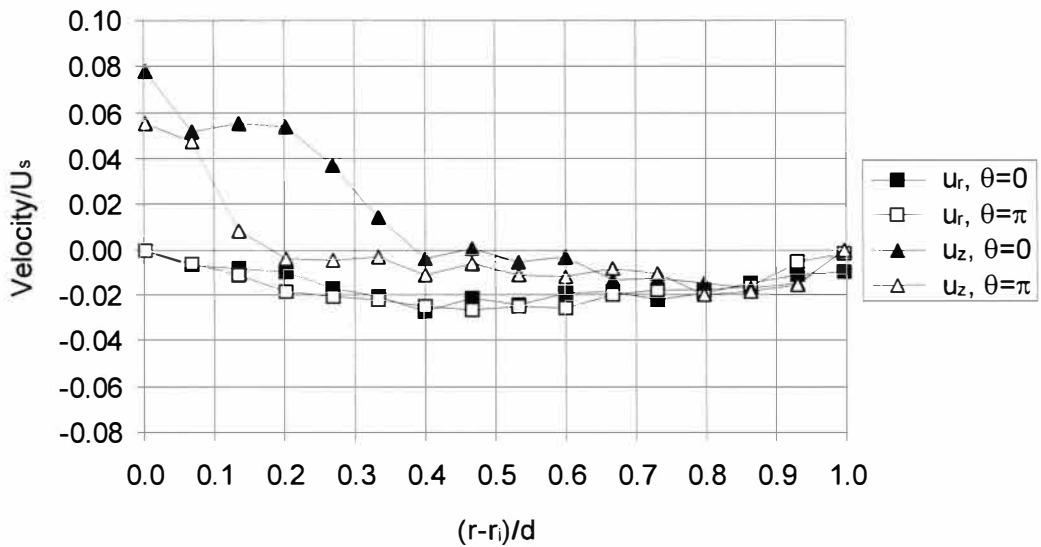

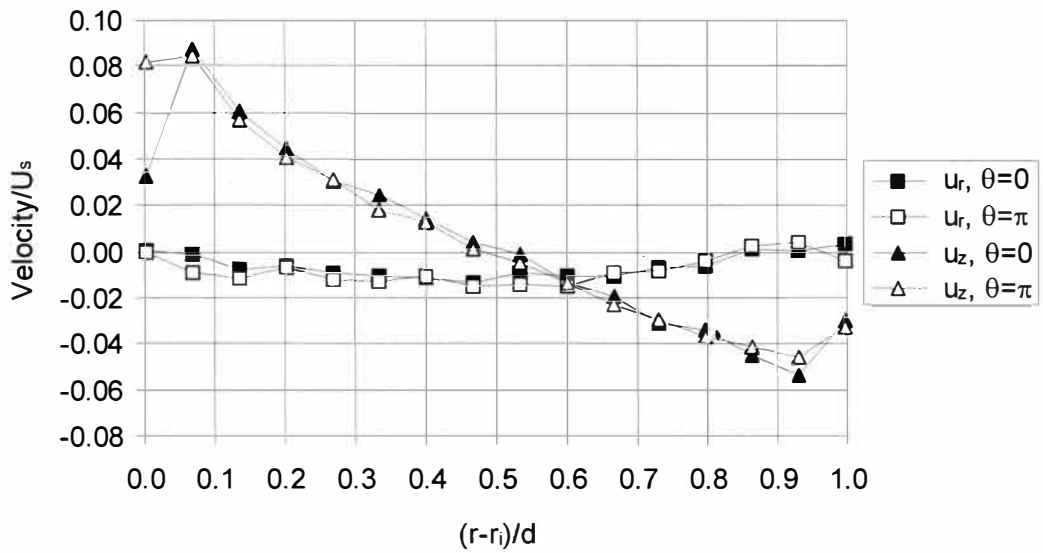Figure 20. Radial and Axial Velocity Comparison, $z/d = 0.13$.

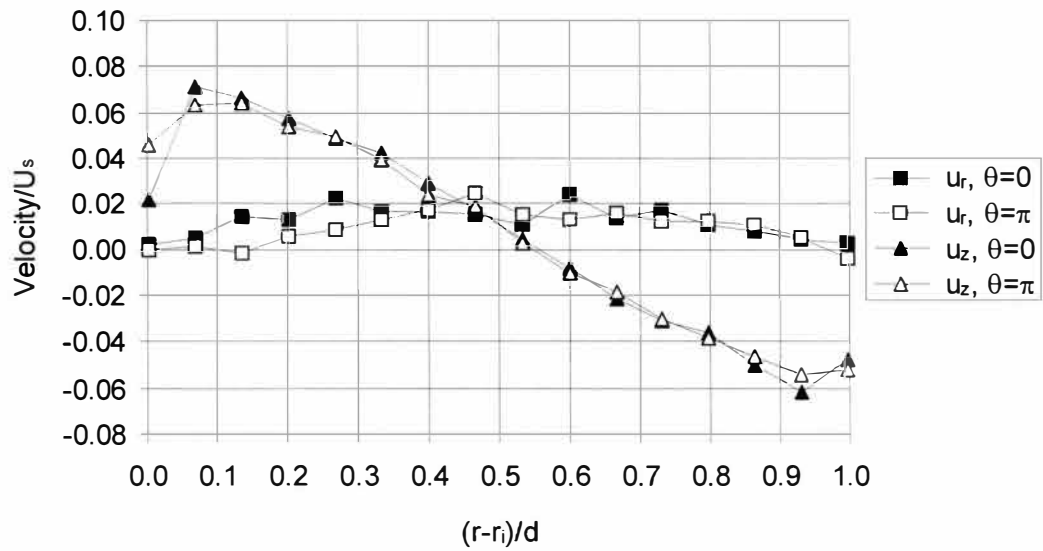Figure 21. Radial and Axial Velocity Comparison, z/d = 0.66.

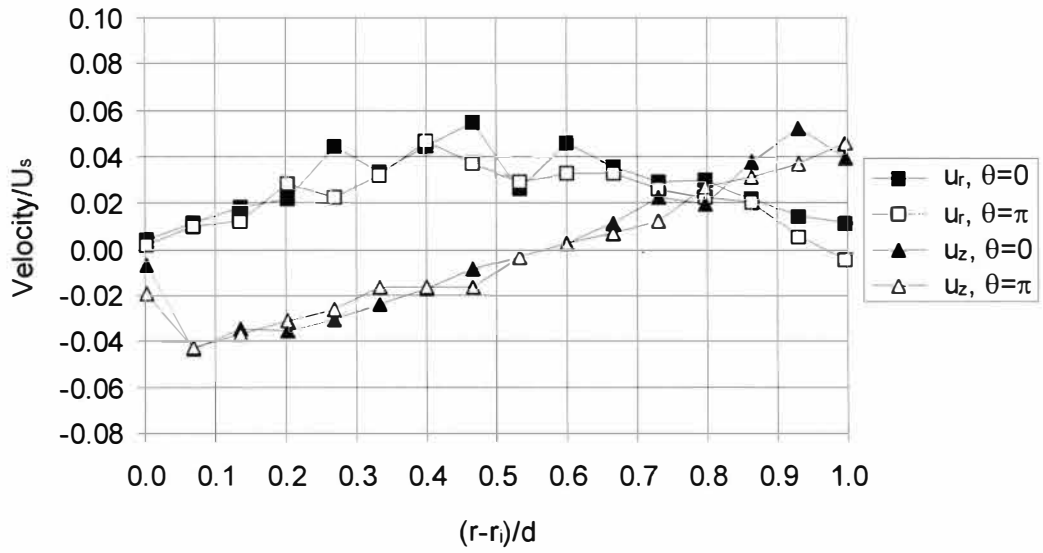Figure 22. Radial and Axial Velocity Comparison, z/d = 1.33.

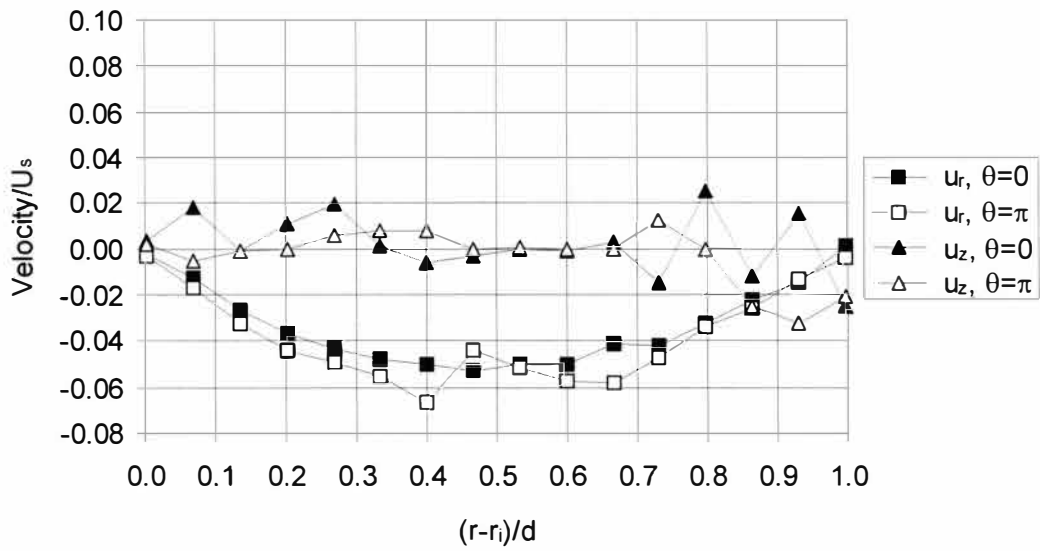Figure 23. Radial and Axial Velocity Comparison, z/d = 1.99.

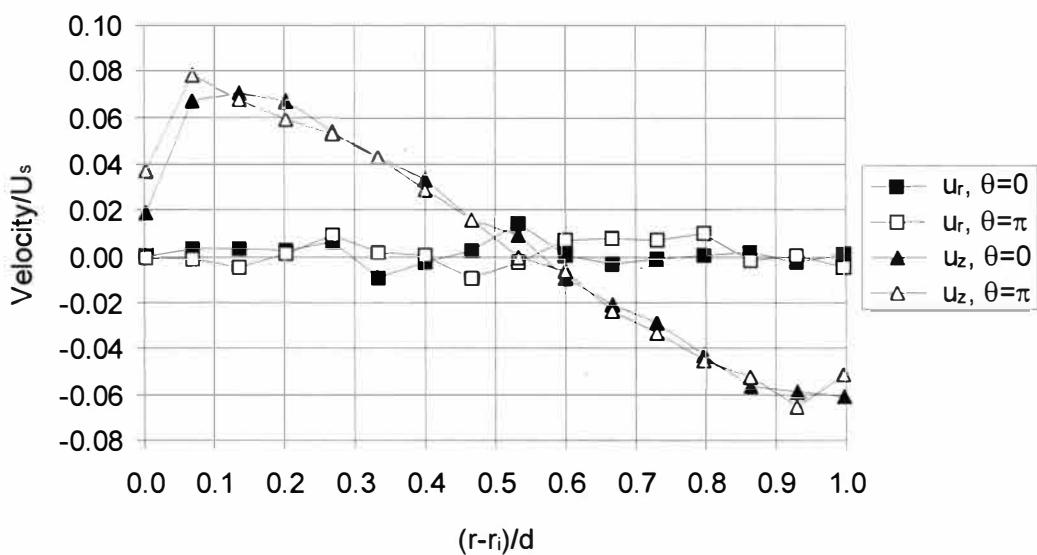Figure 24. Radial and Axial Velocity Comparison, z/d = 2.65.

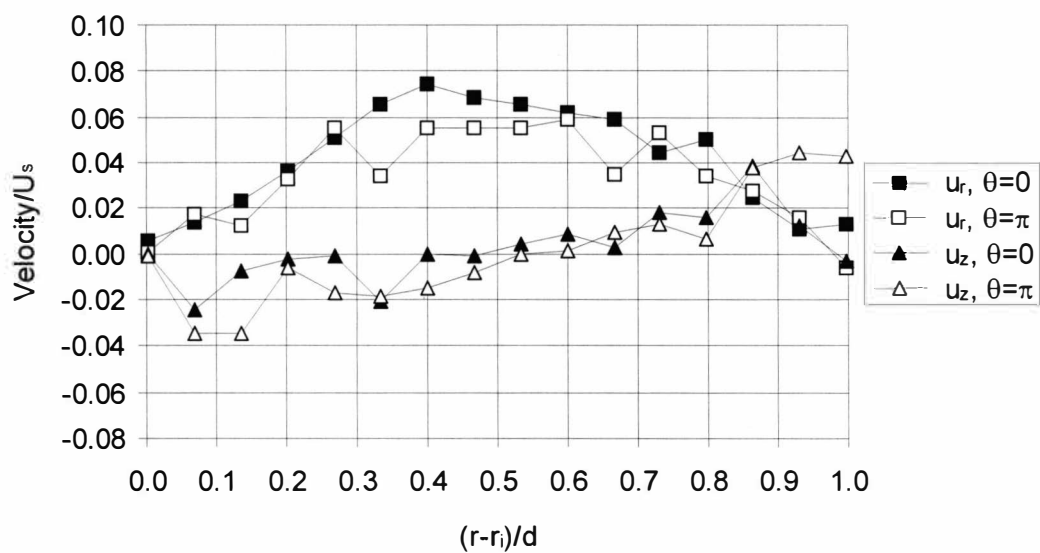Figure 25. Radial and Axial Velocity Comparison, z/d = 3.32.

Figure 26. Radial and Axial Velocity Comparison, z/d = 3.98.
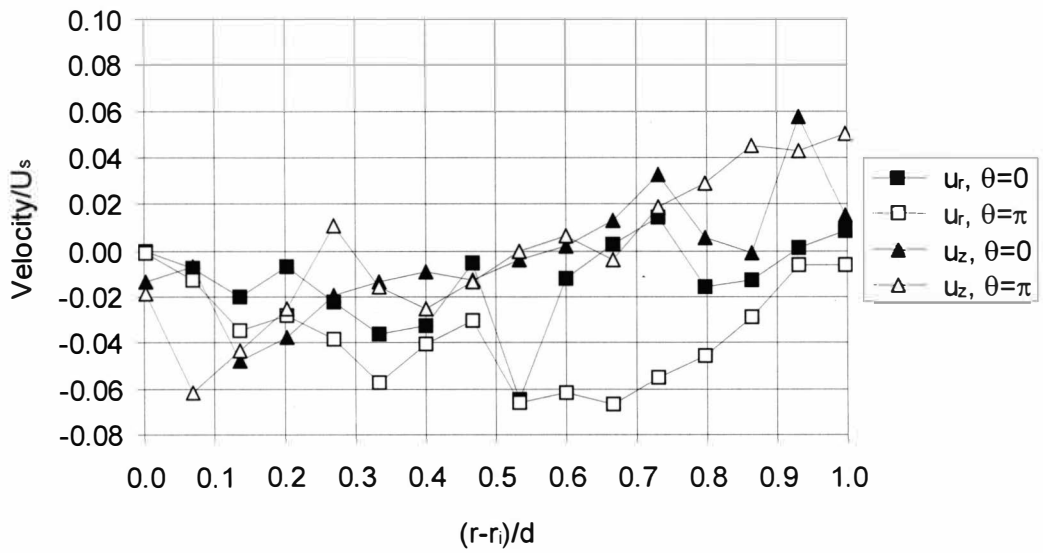
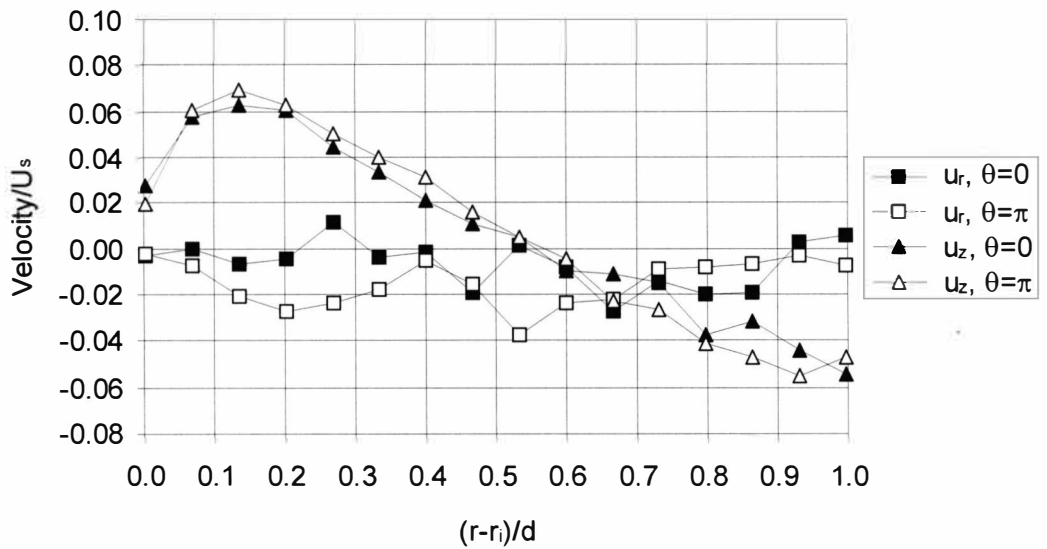Figure 27. Radial and Axial Velocity Comparison, z/d = 4.64.

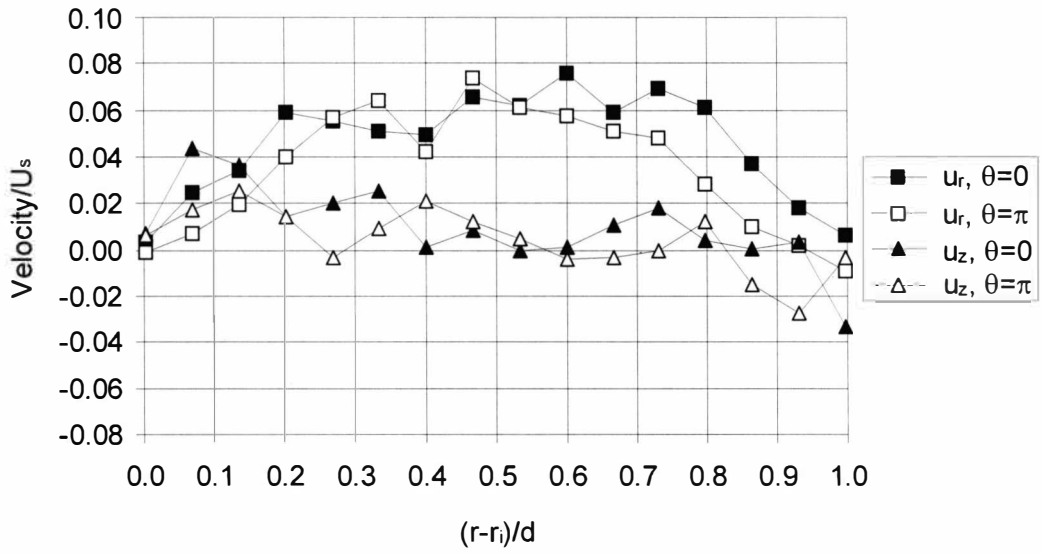Figure 28. Radial and Axial Velocity Comparison, z/d = 5.31.

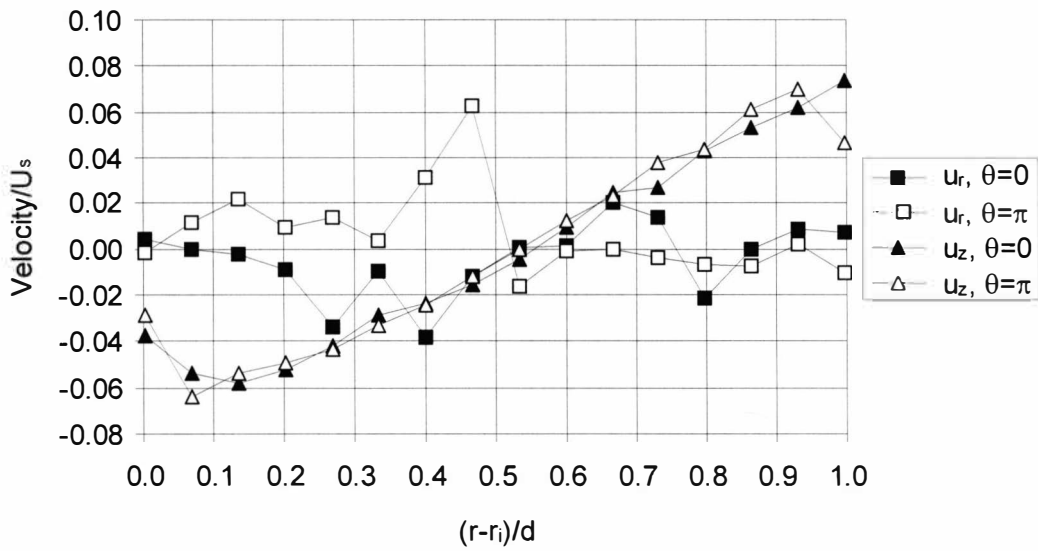Figure 29. Radial and Axial Velocity Comparison, z/d = 5.97.

Figure 30. Radial and Axial Velocity Comparison, z/d = 6.63.

CONCLUSIONS

Refractive index matching provided an annular test apparatus with unrestricted access to the contained turbulent, Taylor-Couette flow. All optical walls were constructed from clear acrylic and, with a very close refractive index match, the only light refraction occurred at the flat housing surface. An aqueous solution of sodium iodide was used to match the 1.4905 refractive index of Plexiglas at 27.0 C. The annulus consisted of a rotating cylinder aligned within a stationary outer cylinder such that the ratio of inner to outer cylinder radii was 0.672. The annulus length was set at 20 and 4 times the annulus gap. The flow Taylor number was 2.107×10^9, the Taylor number ratio $T/T_c = 924,600$, and the Reynolds number was 73,440.

Axial, radial, and azimuthal velocities and turbulence intensities were measured with Laser Doppler Velocimetry along an azimuthal plane while the inner cylinder rotated at 1200 rpm. Axisymmetric mean velocity conditions in the circumferential direction were investigated by measuring the radial and axial velocity components on two radial-axial planes separated by 180 degrees. Velocity vectors and component velocities for the two planes compared very favorably, supporting the theory of azimuthal symmetry of the mean flow.

Radial-axial velocity vector plots and component velocity contours revealed the Taylor vortex structure. With the annulus length set at 20 times the annulus gap, 18 vortices were observed. Three pairs of Taylor vortices were affected by the end

43

walls before the vortices reached a size equilibrium slightly larger than the predicted critical vortex size. With the annulus length set at 4 times the annulus gap, the two resulting vortices were dominated by the stationary end walls, and the overall velocities were reduced with respect to the long annulus. Jet effects were observed in the distribution of the high velocity mean and turbulence intensity into the radial outflow regions and the low velocity mean and turbulence intensity into the radial inflow regions.

BIBLIOGRAPHY

Barnes, N. D., Flitney, R. K., & Nau, B. S. (1992). Mechanical seal chamber design for improved performance. Proceedings of the Ninth International Pump Users Symposium. Houston, Texas.

Braun, M. J., Canacci, V. A., & Hendricks, R. C. (1990). Flow visualization and quantitative velocity and pressure measurements in simulated single and double brush seals. Paper presented at the 45th annual meeting of STLE, Denver, Colorado.

Burkhalter, J. E., & Koschmieder, E. L. (1972). Steady supercritical Taylor vortex flow. Journal of Fluid Mechanics, 58(3), 547-560.

Burkhalter, J. E., & Koschmieder, E. L. (1974, November). Steady supercritical Taylor vortices after sudden starts. Physics of Fluids, 17, 1929-1935.

Chen, R. C., & Kadambi, J. R. (1990). LDV measurements of solid-liquid slurry flow using refractive index matching technique. Particulate Science and Technology, 8, 97-109.

Donnelly, R. (1991, November). Taylor-Couette flow: the early days. Physics Today, 32-39.

Dybbs, A., & Edwards, R. V. (1987, September). Refractive index matching for difficult situations. Paper presented at the Second International Conference on Laser Anemometry - Advances and Applications, Strathclyde, UK.

Fenstermacher, P. R., Swinney, H. L., & Gollub, J. P. (1979). Dynamical instabilities and the transition to chaotic Taylor vortex flow. Journal of Fluid Mechanics. 94(1), 103-128.

Koschmieder, E. L. (1979). Turbulent Taylor vortex flow. Journal of Fluid Mechanics, 93, 515-527.

Koschmieder, E. L. (1993). Benard cells and Taylor vortices. New York: Cambridge University Press.

Merati, P., Jacobs, L., & Parker, J. (1995, January). Particle Image Velocimetry in Taylor-Couette Flow. Paper presented at the Proceedings of the 3rd Fluid Dynamics Conference, Tehran, Iran.

Merati, P., Parker, J., & Adams, W. (1992, September). Turbulent flow of an annulus with inner rotating cylinder and a dead end wall. Paper presented at the Thirteenth Symposium on Turbulence, Rolla, MO.

Northrup, M. A., Kulp, T. J., & Angel, S. M. (1991, July). Fluorescent particle image velocimetry: application to flow measurement in refractive index-matched porous media. Applied Optics, 30, 21, 3034-3040.

Roberts, P. H. (1965, January). The solution of the characteristic value problem. Proceedings of the Royal Society of London, Series A, 283, 550-556.

Smith, G. P., & Townsend, A. A. (1982). Turbulent Couette flow between concentric cylinders at large Taylor numbers. Journal of Fluid Mechanics, 123, 187-217.

Sparrow, E. M., Munrow, W. D., & Jonsson, V. K. (1964). Instability of the flow between rotating cylinders: the wide gap problem. Journal of Fluid Mechanics, 20, 35-46.

Swinney, H. L., & Gollub, J. P. (1985). Hydrodynamic instabilities and the transition to turbulence (2nd ed.). New York: Springer.

Thompson, B. E. (1990, May). Refractive index matching techniques in complex rocket-engine flow configurations. Paper presented as SRA Contractor Final Report R89-900072-F.

Walowit, J., Tsao, S., & DiPrima, R. C. (1964, December). Stability of flow between arbitrarily spaced concentric cylinder surfaces including the effect of a radial temperature gradient. Journal of Fluid Mechanics, 31, 585-593.